A Real-Time Expert Control System For Helicopter Autorotation

Zachary N. Sunberg
Nathaniel R. Miller
Graduate Student
Texas A & M University, College Station, TX

Jonathan D. Rogers*
Assistant Professor
Georgia Institute of Technology, Atlanta, GA

A control algorithm for autonomous helicopter autorotation is proposed and evaluated. The algorithm consists of a multi-phase control law with fuzzily defined transitions and provides outputs in the form of collective commands, desired forward speed, and maximum pitch and roll angle limits. The algorithm is designed to be used in conjunction with an inner loop velocity tracking controller. A unique feature of the proposed control law is its use of estimated time to ground impact to compute near-optimal flare trajectories from a wide range of initial conditions. The performance of the proposed expert control system is evaluated through six degree-of-freedom simulation of both a full-size helicopter and a small hobby-size helicopter, and Monte Carlo examples demonstrate robustness to various initial flight conditions. Limited flight-test results are presented, demonstrating suitable performance of the algorithm in realistic disturbance environments.

Nomenclature

h	altitude above ground level ($-z$), ft
I_R	main rotor polar moment of inertia about shaft, slug-ft^2
$[I_c]_B$	moment of inertia matrix about the center of mass resolved in the body reference frame, slug-ft^2
KE	kinetic energy (slug-(ft/s)^2)
m	helicopter mass, slugs
p, q, r	angular velocity components in body reference frame, rad/s
R	main rotor radius, ft
r	radial distance from rotor hub, ft
u, v, w	mass center velocity components in the body reference frame, ft/s
x, y, z	mass center position components in a north-east-down inertial coordinate system, ft
β	blade flapping angle, rad
$\beta_0, \beta_{1c}, \beta_{1s}$	first harmonic blade flapping angle components, rad
η	total magnitude of vehicle roll and pitch angles; $\eta \equiv \sqrt{\phi^2 + \theta^2}$, rad
$\eta_{\max}$	maximum limit on total magnitude of roll and pitch angles, rad
θ_{tr}	tail rotor collective pitch, rad
θ_0	main rotor collective blade pitch, rad
θ_{1c}	main rotor lateral cyclic pitch, rad
θ_{1s}	main rotor longitudinal cyclic pitch, rad
λ_i	main rotor–induced inflow, nondimensional
$\lambda_0, \lambda_c, \lambda_s$	component states of induced inflow distribution, nondimensional
μ_{small}	membership function defining fuzzy set of small velocities
ϕ, θ, ψ	roll, pitch, and yaw Euler angles, rad
ψ_{MR}	main rotor azimuth angle, rad
Ω	main rotor rotation rate, rad/s

Introduction

When a single engine helicopter encounters engine failure, or when any helicopter suffers a catastrophic transmission or tail rotor failure, an autorotative maneuver must be performed to bring the aircraft to a safe landing. During autorotation, rotor kinetic energy is maintained by extracting energy from air flowing through the main rotor disk in descending flight. The recent rise of autonomous helicopter technology of various scales has led to new demand for automatic control systems that can perform autorotation manuevers autonomously as part of the flight control system. Incorporation of an autonomous autorotation control capability enhances overall system safety and may improve prospects for integration of autonomous helicopters into the National Airspace System on a large scale. In manned aircraft, an autorotation controller may be used as part of an avionics system to provide pilot guidance in emergency situations, degraded visual environments, or in difficult scenarios in which the maneuver is initiated inside the "deadman's curve" region of the height–velocity (H–V) diagram (Ref. 1).

Autonomous autorotation controllers have been studied by several investigators, although few have been fielded in production systems to date. An early study of the autorotation problem from an automatic control perspective is provided by Johnson (Ref. 2). In this work, optimal descent trajectories and a nonlinear controller using an offline gradient descent approach are used to minimize the predicted total velocity at impact, but the results are intended to be used for vehicle design rather than real-time feedback control. Lee et al. (Ref. 3) improved on this initial analysis by adding constraints relating to physical performance

*Corresponding author; email: jonathan.rogers@me.gatech.edu.
Manuscript received September 2013; accepted August 2014.

limits to the optimization problem and evaluating initial conditions well within the height–velocity avoid region. This analysis concluded that the flight envelope for safe autorotation can be significantly enlarged using automatic control. More recently, in research focused on autonomous rotorcraft, Hazawa et al. (Ref. 4) created a traditional proportional–integral controller for landing a small helicopter in cases of engine failure. Abbeel et al. (Ref. 5) created a reinforcement learning controller that attempts to match trajectories recorded from autorotative descents performed by a human pilot. Algorithm performance was verified experimentally during successful autonomous autorotations executed with a small hobby-sized helicopter. Dalamagkidis et al. (Ref. 6) developed an autorotation control system based on receding horizon neural network optimization, although the controller was limited to vertical autorotations only and was tested in simulation using a simplified one-dimensional dynamic model. These tests were further restricted in the case of full-scale aircraft to include only vehicles modified with a high-energy rotor system (Ref. 7), providing a high margin for error in control system performance.

Additional research has focused on control automation during specific phases of descent or for vehicle path planning. Yomchinda et al. (Ref. 8) have proposed a path-planning algorithm for the steady-state descent phase, whereas Tierney and Langelaan (Ref. 9) have presented a method for calculating the set of flare entry points from which a helicopter can safely land. Others have developed methods to reduce pilot workload during autorotation using simple heuristic criteria that communicate to a pilot upon approaching a dangerous state (Ref. 10). Recently, Bachelder et al. (Ref. 11) developed an autonomous autorotation controller based on iterative optimization. The control law was implemented in an avionics package and was meant to provide pilot cues and guidance during autorotative descents.

Many elements common to previous approaches have limited their utility in practical systems. Reinforcement learning algorithms require extensive training data that may not be available, and since they are tied to a specific flight platform they are limited in flexibility and scalability to other aircraft. Iterative optimization algorithms, such as those proposed in Refs. 6, 8, and 11, require significant computational capability and in general lack convergence guarantees. Such iterative algorithms may not be suitable for certification, especially given the time constraints inherent in autorotation trajectory generation and the robustness guarantees likely to be required. Throughout the autorotation control literature, it has been almost universally recognized that computation of a feasible flare trajectory is one of the most difficult control tasks inherent in the maneuver given the variety of initial flight conditions, the presence of external disturbances, and the high dimensionality of the problem (Ref. 9). Especially for low-cost platforms, new autorotation control laws are needed that provide suitable flexibility and robustness while avoiding iterative optimization, high-fidelity onboard dynamic models, or black box reinforcement learning approaches.

At the same time, significant recent research efforts in the handling qualities community led by Padfield et al. (Refs. 12–14) have noted the importance of estimated time to contact with a point or obstacle in a wide variety of pilot maneuvers. This value, termed optical tau and defined as the ratio between distance to a certain viewpoint and closing velocity, has been demonstrated to be a critical factor in pilot trajectory tracking, evasive maneuvers, and pilot-induced oscillation. Specifically, Jump and Padfield (Ref. 15) have shown that, during flare maneuvers close to the ground, pilots adjust the estimated motion tau to ground impact through control inputs to match a pilot-generated reference value. Similarly, it is shown here that predicted time to impact with the ground plays an important role in autorotation control and is the mechanism that provides flexibility in flare trajectory generation and tracking.

This paper presents a novel multiphase expert control system for helicopter autorotation. The controller is composed of multiple phases, which are executed sequentially as the autorotation maneuver progresses. Phase changes are fuzzily defined and are initiated through altitude and predicted time-to-impact criteria. A novel aspect of the control design is its use of time-to-impact predictions during the flare maneuver and its use of a desired time-to-impact reference value conditioned on the vehicle's horizontal velocity, vertical velocity, and rotor kinetic energy. A set of tuning parameters allows the controller to be applied to a wide set of helicopter platforms with minimal structural changes. Furthermore, the simplicity of the controller design minimizes computational burden and improves its prospects for flight certification. First, the control system is described in detail, followed by a brief description of the simulation model used to evaluate controller performance. Monte Carlo simulation results are presented for both the Bell AH-1G helicopter as well as for a small remote-controlled (R/C) sized helicopter. Finally, results from a limited set of flight experiments are provided to demonstrate controller performance in a realistic environment.

Control Law Formulation

The control law is designed based on several requirements and design principles. First, it must be applicable to forward flight scenarios and should not be restricted to vertical autorotation only. Second, the control law must not rely on a high-fidelity dynamic model of the aircraft, which may not be available or may be too computationally expensive. Third, the controller should be portable to various classes of helicopters, both manned and unmanned. Finally, the controller should avoid iterative optimization and exhibit minimal computational burden. This final design constraint is meant to allow the autorotation controller to function on many low-cost autopilot systems, which are becoming increasingly popular in the small unmanned aerial vehicle (UAV) community.

These design principles led to formulation of the autorotation controller as an expert system. The term "expert system" has been used to describe a wide range of control systems and other computational structures. Essentially, two characteristics define expert system control architectures. First, such controllers generally imitate control methodologies applied by expert human operators. Second, these control systems usually have "expert" knowledge already available to them at runtime in the form of a deterministic low-order dynamic model, that is, there is no iterative learning, high-fidelity model prediction, or optimization at runtime. An example of an expert control law applied to a similar problem is the controller derived by Livchitz et al. (Ref. 16) for autonomous landing of a small fixed-wing aircraft. Unlike the controller described in Ref. 16, which relies mainly on a fuzzy logic structure, the controller proposed here uses a combination of several reasoning approaches including crisp logic, fuzzy logic, and proportional-integral-derivative control.

The control structure considered in this paper consists of a standard inner-outer loop control architecture, in which an inner-loop controller is responsible for tracking velocity commands generated by an outer loop controller. A block diagram of this control architecture is shown in Fig. 1. During nominal powered operating scenarios, a waypoint following controller may send velocity commands to the inner loop controller (labeled as a "velocity-tracking controller"), which is responsible for achieving a suitable vehicle orientation to track these commands. The inner-loop controller therefore generates main rotor cyclic and collective commands as well as tail rotor collective commands given desired velocity values. In the case of autorotation, the outer loop waypoint following controller is replaced by the autorotation controller described here. The autorotation controller therefore provides forward velocity commands (u_{des}), maximum pitch and roll orientation limits ($\eta_{\max}$), and main rotor collective commands ($\dot{\theta}_0$), as shown in Fig. 1. The velocity commands and orientation constraints are sent directly to the inner-loop controller for tracking. Thus the autorotation control system is designed for straightforward

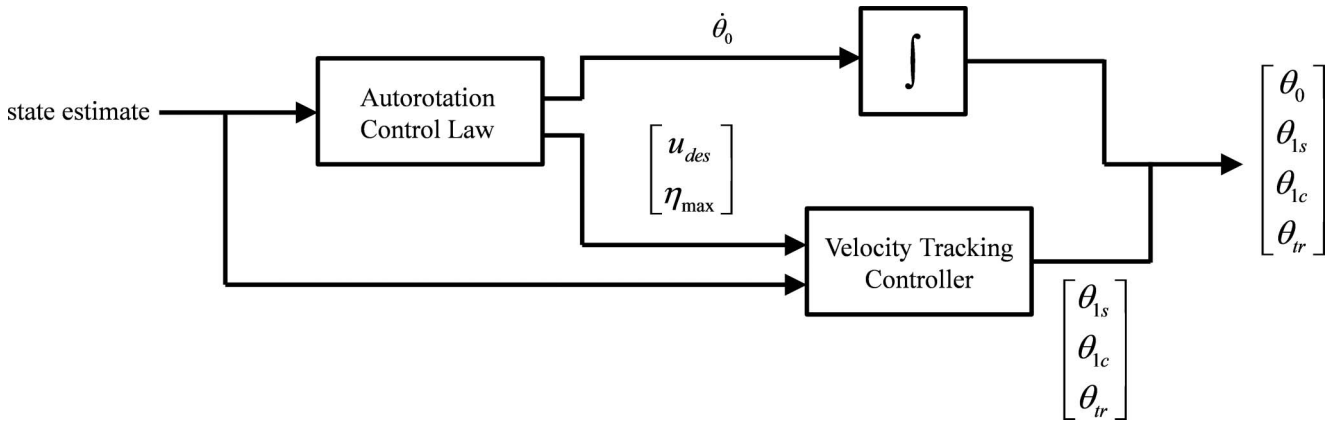

Fig. 1. Control system block diagram. The autorotation control law determines main rotor collective, desired forward speed, and maximum pitch and roll limits for tracking by an inner-loop velocity tracking controller.

integration with an existing inner loop autopilot controller. Note that an autorotation path planning scheme, such as that developed in Ref. 8 for landing site selection, may also be incorporated as an additional outer loop that feeds desired waypoint data to the autorotation control (although such extensions are not explored here). Further note that the controller outputs a maximum orientation angle limit $\eta \equiv \sqrt{\phi^2 + \theta^2}$, which is the total magnitude of the vehicle pitch and roll angles, to simplify the controller structure. While this does not limit the generality of the control design, for many applications it may be desired to specify separate maximum roll and maximum pitch limits. This can certainly be accomplished within the proposed architecture by adding an additional output to the controller in each phase.

The autorotation maneuver is divided into several fuzzily defined phases based on altitude h and the estimated time to ground impact assuming constant velocity, $TTI_{\dot{h}=0} \equiv -h/\dot{h}$. A specific control law is defined for each phase, and phase transitions are initiated by predetermined criteria on altitude and time to ground impact defined for a specific aircraft. The five maneuver phases selected for the controller are termed the steady-state descent, preflare, flare, landing, and touchdown phases (although other phases may be selected, this set of five phases was shown to provide suitable flexibility and robustness through extensive simulation and limited flight experiments). Boundaries between each phase are defined in the altitude and time-to-impact domains through a strict fuzzy partition using trapezoidal membership functions. Figure 2 shows the definition of the phases using example transition values chosen for the Bell AH-1G Cobra. Note that there is an "OR" relationship between the altitude and time to impact phase definitions such that the controller will advance to the next phase if either, or both, of the altitude and time to impact criteria are met. As the autorotation maneuver progresses, forward phase transitions are initiated sequentially and backward transitions (i.e., preflare to steady-state descent) are not allowed, even if altitude increases. This prohibition on backward progression through the phases means that there is not necessarily a unique mapping from the physical state of the helicopter at a given time to a control output. Instead, the control output also depends on the internal controller state or, equivalently, the time history of the helicopter physical state.

Control system phases are defined in a fuzzy manner, meaning that transitions between phases are not "crisp" like a switching control but rather happen over a finite time period (hence the blurred lines in Fig. 2). Use of a fuzzy transition helps to avoid control transients caused by abruptly switching to a different phase control law. A phase control authority value for each phase is defined between 0 and 1, representing the extent to which that phase is active. For instance, when transitioning

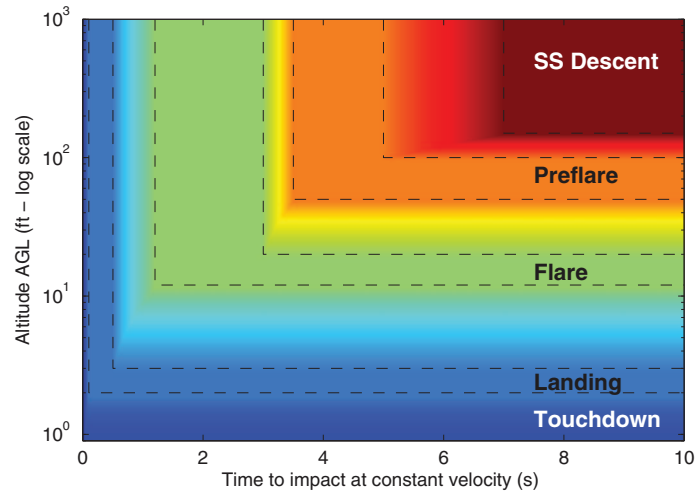

Fig. 2. Example autorotation controller phase diagram. Dashed lines denote the beginning and end of transitions. The regions that contain text are flat regions of the contour, except for the region labeled "touchdown" because the touchdown membership function only reaches saturation at ground level.

from landing to touchdown, the phase control authority value for landing will start at 1 and transition continuously to zero. Likewise, the phase control authority value for touchdown will start at zero and transition continuously to 1. When two phases are partially active, control outputs from each phase are blended together linearly using the phase control authority values as weights. An extensive description of fuzzy control and its advantages is provided in Ref. 17.

A detailed discussion of each of the phase control laws follows. Note that throughout this section, controller tuning parameters are indicated by use of a fixed-width teletype font with underscores, e.g., `U_AUTO`.

Steady-state descent

In the steady-state descent phase, the controller attempts to manage rotor rotational energy in descending flight while the vehicle maneuvers to a suitable landing site. During the descent, a pilot or a path-planning algorithm (such as that developed in Ref. 8) may provide speed and orientation commands, and thus the autorotation controller simply passes these commands to the velocity-tracking controller while managing

collective directly. Since integration of a path planner is beyond the scope of this study, a constant forward speed U_AUTO is commanded and no limits are placed on helicopter orientation outside of those used in the velocity-tracking controller. Therefore, the following equations describe control outputs for this phase:

$$u_{\text{des}} = \text{U\_AUTO} \tag{1}$$

$$\eta_{\max} = \text{limited only by velocity-tracking controller} \tag{2}$$

$$\dot{\theta}_0 = \text{K\_D\_SS}\,\dot{\Omega} + \text{K\_P\_SS}(\Omega - \text{RPM\_AUTO}) \tag{3}$$

where RPM_AUTO is the desired rotor rotational rate in steady-state descent, and K_D_SS > 0, K_P_SS > 0 are user-defined gains. Note that the commands provided in Eqs. (1) and (2) may be replaced by those generated by a human pilot or path-planning algorithm. In the absence of a path-planning algorithm or pilot guidance, U_AUTO may be set to the forward flight speed, which minimizes total power required, therefore minimizing the steady-state descent rate. The RPM_AUTO setpoint value is typically 80–120% of the nominal operating rotor rotation rate (Ref. 1). As shown in Eq. (3), the derivative of collective pitch $\dot{\theta}_0$ is governed by a simple proportional derivative (PD) controller, which drives collective toward a value corresponding to trimmed autorotation. The gains K_D_SS and K_P_SS can be chosen to yield a reasonable response using simplified or high-fidelity dynamic flight simulation. In general, if gains are chosen appropriately this control law will be stable in the normal operating region where the steady-state rotor rotation rate will decrease if θ_0 increases, that is $\partial\Omega_{\text{SS}}/\partial\theta_0 < 0$. The only foreseeable case where this condition might be violated is when a large negative collective (only available on small hobby-sized aerobatic helicopters) is commanded, which forces the helicopter to accelerate downward and the rotor rotation to slow. This can be avoided by placing a positive lower bound on the collective during autorotation if needed.

The steady-state control law is designed to maintain an appropriate rotor rotational rate regardless of the forward speed of the helicopter or maneuvers used to reach a safe landing site. This makes it suitable for use in piloted flight (where the pilot controls cyclic commands) or with higher level path-planning algorithms. Simulation tests have shown that the controller is able to adjust θ_0 to suit a range of steady-state forward speeds.

Preflare

During the preflare phase, the controller attempts to bring the helicopter state into the subspace that will likely result in a successful flare maneuver. The preflare controller is identical to the steady-state descent controller except that it places limits on the total vehicle orientation angle η to avoid aggressive maneuvers when entering the flare phase. The following equations define control outputs for this phase:

$$u_{\text{des}} = \text{U\_AUTO} \tag{4}$$

$$\eta_{\max} = \text{PRE\_FLARE\_MAX\_ANGLE} \tag{5}$$

$$\dot{\theta}_0 = \text{K\_D\_SS}\,\dot{\Omega} + \text{K\_P\_SS}(\Omega - \text{RPM\_AUTO}) \tag{6}$$

Once again, appropriate velocity commands may be substituted for U_AUTO given pilot guidance or a path-planning algorithm.

Flare

The flare maneuver is the most critical aspect of the autorotation, and proper timing is vital. The goal of the flare phase is to reduce the vertical and horizontal velocities to values suitable for safe entry into the landing phase. To that end, the desired horizontal velocity is set to a small reference value U_TOUCHDOWN and η is not limited to provide the velocity-tracking controller enough flexibility to achieve U_TOUCHDOWN as quickly as possible. Thus the desired velocity and orientation limits in the flare phase are given by

$$u_{\text{des}} = \text{U\_TOUCHDOWN} \tag{7}$$

$$\eta_{\max} = \text{limited only by velocity-tracking controller} \tag{8}$$

The remaining task for the autorotation controller is to determine and track a vertical trajectory that will cause the helicopter to enter the landing phase at the same time that the aircraft velocity reaches U_TOUCHDOWN. Determining a feasible flare trajectory is noted as a challenge in the literature (Ref. 5). Instead of attempting to directly specify a feasible trajectory in the helicopter's physical state space, the problem is transformed into a new time-to-impact domain that lends itself to a heuristic reasoning approach for trajectory generation. Four important variables in the time-to-impact domain are used by the controller given by (1) $TTI_{\ddot{h}=0}$, the estimated time to ground impact assuming constant vertical speed, (2) TTI_L, the desired time to ground impact during the landing phase, (3) *TTLE*, the desired time to landing phase entry, and (4) TTI_F, the desired time to ground impact during the flare phase. These four variables, summarized in Table 1, allow the flare trajectory to be generated in a robust and flexible manner based on state feedback. Note that $TTI_{\ddot{h}=0}$, *TTLE*, and TTI_F are computed directly from feedback values, whereas TTI_L is a constant controller tuning parameter.

Table 1. Time to Impact Variables and parameters used in the flare control law

Variable	$TTI_{\ddot{h}=0}$ (horizontal axis in Fig. 2)
Physical meaning	Estimated *T*ime-*T*o-*I*mpact assuming speed remains constant
Source	Calculated as $-h/\dot{h}$
Use	Determining controller phase
Variable	TTI_L
Physical meaning	*Desired T*ime-*T*o-*I*mpact during the *L*anding phase
Source	Tunable control law parameter
Use	Landing phase control law and determining TTI_F
Variable	*TTLE*
Physical meaning	*Desired T*ime-*T*o-*L*anding phase *E*ntry
Source	Determined by algorithm in Eq. (13)
Use	Determines TTI_F
Variable	TTI_F
Physical meaning	*Desired T*ime-*T*o-*I*mpact during the *F*lare phase
Source	$TTI_F \equiv \text{TTI\_L} + TTLE$
Use	Flare phase closed-loop control law

Example values for each parameter are shown in the Simulation Results section.

The introduction of the time-to-impact domain, the tasks of the flare phase controller are to prescribe a suitable target value for *TTLE* using a heuristic rule set and to apply control inputs that will put the helicopter on a trajectory to enter the landing phase approximately *TTLE* seconds in the future. Further clarity regarding the meaning and computation of these time-to-impact parameters is provided in the following discussion.

Prescription of TTLE. The desired time to landing entry is conditioned on the amount of kinetic energy available to the helicopter to perform maneuvers. Given sufficient rotor rotational kinetic energy, or sufficient forward flight speed, the descent can be more gradual and *TTLE* may be larger. Conversely, if little kinetic energy is available, the helicopter must flare more abruptly, and thus *TTLE* should be smaller to

enter the landing phase sooner. Thus, *TTLE* is scaled between 0 and TTI_F_MAX − TTI_L using a scale factor derived from the total kinetic energy available for maneuver. Define total kinetic energy as the sum of the kinetic energy due to vehicle forward velocity and that due to rotor rotational kinetic energy according to

$$KE_{\text{available}} \equiv \frac{1}{2}mu^2 + \frac{1}{2}I_R\Omega^2 \tag{9}$$

Furthermore, define the target kinetic energy at flare entry and exit as

$$KE_{\text{flare entry}} \equiv \frac{1}{2}m(\text{U\_AUTO})^2 + \frac{1}{2}I_R(\text{RPM\_AUTO})^2 \tag{10}$$

$$KE_{\text{flare exit}} \equiv \frac{1}{2}m(\text{U\_TOUCHDOWN})^2 + \frac{1}{2}I_R(\text{RPM\_AUTO})^2 \tag{11}$$

Thus a scale factor may be defined relating the current kinetic energy to the desired values at flare entry and exit according to

$$\alpha \equiv \frac{KE_{\text{available}} - KE_{\text{flare exit}}}{KE_{\text{flare entry}} - KE_{\text{flare exit}}} \tag{12}$$

Finally, time to landing phase entry *TTLE* is calculated as

$$TTLE = TTLE_{\max} \times \min(1,\ \max(0,\ \alpha)) \tag{13}$$

where $TTLE_{\max} \equiv$ TTI_F_MAX−TTI_L. Note that in cases of very low total kinetic energy, when $KE_{\text{available}}$ is less than $KE_{\text{flare exit}}$, $TTLE = 0$ and thus an immediate transition to the landing phase is initiated. If kinetic energy is very high (greater than $KE_{\text{flare entry}}$), the time to landing phase entry is given by the tuning parameter TTI_F_MAX − TTI_L, providing a longer and more gradual flare trajectory. The computed *TTLE* is used to prescribe the desired time to impact for the flare phase, TTI_F, according to the following formula:

$$TTI_F = TTLE + \text{TTI\_L} \tag{14}$$

Note that values for *TTLE* and TTI_F are continually calculated at a high rate during the flare maneuver using feedback measurement data, allowing rapid adjustment of the flare trajectory and compensating for disturbances such as winds, which may significantly alter kinetic energy available.

Flare trajectory tracking. Once the desired time to impact required for vertical deceleration, TTI_F, has been calculated as described above, a vertical trajectory to the ground is generated. During flare trajectory generation, the vertical flight path is parameterized using a constant acceleration model. Although a desired constant acceleration is computed, it is updated at a high rate based on feedback measurements and thus a time-varying acceleration profile results. Let the vehicle altitude above ground at time t be given as $h(t)$ and vertical velocity as $\dot{h}(t)$. With constant vertical acceleration $\ddot{h}(t)$, the altitude at time $t + TTI_F$ is given by

$$h(t + TTI_F) = h(t) + \dot{h}(t)\,TTI_F + \frac{1}{2}\ddot{h}(t)\,TTI_F^2 \tag{15}$$

Setting $h(t + TTI_F) = 0$ yields a desired constant acceleration value of

$$\ddot{h}_{\text{des}} = -\frac{2}{TTI_F^2}h - \frac{2}{TTI_F}\dot{h} \tag{16}$$

Equation (16) essentially guarantees that $t + TTI_F$ will be a root of Eq. (15), but does not guarantee that another root does not exist at a time before $t + TTI_F$. This additional root exists in a trajectory that crosses the ground plane in the downward direction before $t + TTI_F$ and then crosses the ground plane in the upward direction again at $t + TTI_F$ (with $\dot{h}(t + TTI_F) > 0$). The condition on TTI_F, which guarantees that the first intersection of the trajectory with the ground plane occurs at $t + TTI_F$ (i.e., the desired behavior), is given by

$$TTI_F \le \frac{-2h}{\dot{h}} \tag{17}$$

If Eq. (17) is not satisfied, no constant acceleration command will yield a root of Eq. (15) with $\dot{h}(t + TTI_F) < 0$. These two possibilities, given by satisfaction and violation of the inequality in Eq. (17), are treated separately in the flare phase control law.

Assuming that Eq. (17) is satisfied, collective commands must be generated to achieve $\ddot{h}_{\text{des}}$ computed from Eq. (16). The complexity of rotor aerodynamics in general prohibits a simple mapping between collective pitch and corresponding thrust values due to numerous effects such as blade stall, tip and root losses, inflow dynamics and spatial variation, ground effect, and other aerodynamic phenomena. For this reason, the controller uses acceleration feedback measurements to dynamically adjust the collective to attain the proper vertical acceleration. A simple model to guide this adjustment may be created by assuming low disk loading, linear aerodynamics, uniform inflow, constant chord blades, and zero twist. Using these simplifications, an expression for the thrust coefficient may be generated as (Ref. 1)

$$C_T = \sigma c_{l_\alpha}\left(\frac{\theta_0}{6} - \frac{\lambda}{4}\right) \tag{18}$$

where C_T is thrust coefficient, σ is rotor solidity, c_{l_α} is blade section lift curve slope, and λ is nondimensional inflow. Dimensionalizing this expression, adding gravitational effects, and neglecting horizontal components of rotor thrust yields a linear relationship between collective and vertical acceleration given by

$$\ddot{h} = \rho R^3\Omega^2 Nc\left(\frac{\theta_0}{6m} - \frac{w}{4m\Omega R}\right) + g \tag{19}$$

Here ρ is atmospheric density, N is number of main rotor blades, c is blade chord, w is rotor inflow, and g is gravitational acceleration. While there is significant uncertainty in this relationship introduced by the various assumptions outlined in Ref. 1, it establishes the general trend that an increase in collective pitch generates a proportional increase in vertical acceleration, where the constant of proportionality is unknown and varies according to flight condition and other factors. Referencing Eq. (19), let θ_0^D be the (unknown) collective command that achieves $\ddot{h}_{\text{des}}$ given the current inflow state, and let θ_0^C be the collective command at time t yielding $\ddot{h}(t)$. Then a simple proportional control law may be established that drives the collective pitch toward the desired value according to

$$\dot{\theta} = k_{\theta_0}\left(\theta_0^D - \theta_0^C\right) = \frac{\text{K\_COL}}{\text{TAU}}(\ddot{h}_{\text{des}} - \ddot{h}) \tag{20}$$

where k_{θ_0} is a positive constant and K_COL > 0 and TAU > 0 are user-defined tuning parameters. Thus, using the right-hand side of Eq. (20), collective is adjusted in the direction of the desired value until the desired vertical acceleration is achieved. Clearly, K_COL and TAU are redundant parameters and may be combined into a single value. However, given the linear relationship in Eq. (19), K_COL may be tuned according to the approximation

$$\text{K\_COL} \approx \frac{6m}{\rho R^3\Omega^2 Nc} \tag{21}$$

which are all known parameters of the helicopter geometry and operating environment. TAU may then be adjusted to influence the speed of the control response.

If the condition in Eq. (17) is not met, it is not possible to compute a constant acceleration which leads to ground impact at time $t + TTI_F$. In such a flight regime, use of the acceleration expression in Eq. (16) yields a root of Eq. (15) that occurs at a time before $t + TTI_F$, meaning that the helicopter will impact the ground too soon. To prevent this, if the condition in Eq. (17) is violated, the flare phase controller commands a large upward adjustment of the collective pitch (given by the controller parameter FAST_COL_INCREASE). This is analogous to a human pilot sensing that the magnitude of the vertical velocity is too large and, in response, rapidly increasing the collective pitch until the velocity has reached a suitable value for satisfaction of Eq. (17).

Equation (22) summarizes the implementation of the collective portion of the flare phase control law. This equation combined with Eqs. (7), (13), and (14) creates a complete description of the flare phase control law:

$$\dot{\theta}_0 = \begin{cases} \frac{\text{K\_COL}}{\text{TAU}} \left(-\frac{2(h + \dot{h} TTI_F)}{TTI_F^2} - \ddot{h} \right) & \text{for} -\frac{2h}{\dot{h}} \geq TTI_F \\ \text{FAST\_COL\_INCREASE} & \text{for} -\frac{2h}{\dot{h}} < TTI_F \end{cases} \tag{22}$$

Landing

In the landing phase, the controller seeks to approach the ground gently with nearly level attitude. The control law is similar to the flare phase control law (derived from Eqs. (16) and (20)), except that the desired time to impact remains at a constant value given by the controller parameter TTI_L. An example value of TTI_L = 2.0 s was found to be suitable for the AH-1G through simulation experiments. Thus the landing phase control law is given by

$$u_{\text{des}} = \text{U\_TOUCHDOWN} \tag{23}$$

$$\eta_{\max} = \text{LANDING\_MAX\_ANGLE} \tag{24}$$

$$\dot{\theta}_0 = \begin{cases} \frac{\text{K\_COL}}{\text{TAU}} \left(-\frac{2(h + \dot{h}\,\text{TTI\_L})}{\text{TTI\_L}^2} - \ddot{h} \right) & \text{for} -\frac{2h}{\dot{h}} \geq \text{TTI\_L} \\ \text{FAST\_COL\_INCREASE} & \text{for} -\frac{2h}{\dot{h}} < \text{TTI\_L} \end{cases} \tag{25}$$

Touchdown

The touchdown phase brings the helicopter to rest on the ground by decreasing the collective slowly and attempting to maintain a level orientation. For large helicopters, limits on the control inputs may need to be implemented in this phase to keep the blades from impacting the fuselage or empennage after touchdown due to potentially low rotor rotation rates, although these limits have not been included here and would be highly vehicle dependent. The touchdown phase control law is given by

$$u_{\text{des}} = \text{U\_TOUCHDOWN} \tag{26}$$

$$\eta_{\max} = \text{TOUCHDOWN\_MAX\_ANGLE} \tag{27}$$

$$\dot{\theta}_0 = \text{TOUCHCOWN\_COL\_DECREASE} \tag{28}$$

A total of 10 controller parameters are defined in the preceding sections. In the testing performed as part of this study, it was observed that controller response is relatively insensitive to adjustments in almost all of these parameters with the notable exception of K_COL and TAU, which are fundamental to shaping the flare trajectory. A summary of each of the controller parameters is provided in Tables 2 and 3, as well as example values for the AH-1G and a small R/C size helicopter derived through simulation studies. Note that these parameters may be reliably determined from low-to-medium fidelity rotorcraft simulation models such as the one described in the following section. Further note that separate pitch and roll angle parameters may be added, as well as separate limits for positive and negative angles, if desired during practical implementation. However, it was observed that these parameters do not significantly affect performance as long as the inner-loop control law is adequately tuned.

Alternate acceleration-free control law

The flare and landing phase collective control laws specified in Eqs. (22) and (25) require vertical acceleration feedback. On some low-cost flight platforms, including the R/C model used in experimental studies performed here, accurate acceleration feedback with suitable noise characteristics is difficult to obtain at high update rates. In this case, an alternative, acceleration-free control law formulation is desired. The modified collective control law derived here differs from that shown above only in the trajectory tracking portion of the flare and landing phases. This modified controller uses the same methods to determine $TTLE$ and TTI_F described previously; however, instead of specifying $\dot{\theta}_0$ as shown in Fig. 1, θ_0 is computed directly. This modified control law attempts to follow an exponentially decaying altitude profile to ground impact.

Consider vertical trajectory dynamics as shown in Eq. (19). Assuming inflow changes occur slowly compared to the controller update rate, inflow can be treated in a quasi-static manner and Eq. (19) can be rewritten in a simplified form as

$$\ddot{h} = \frac{1}{K_{\theta_0}} (\theta_0 - G) \tag{29}$$

where G accounts for both the inflow and gravity terms. Equation (29) is a linear second-order differential equation in terms of h. Now consider a feedback control law of the following form:

$$\theta_0 = K_{\theta_0} \left(\frac{1}{\tau_C} \left(-\frac{h}{\tau_T} - \dot{h} \right) - \frac{h}{\tau_T} + G \right) \tag{30}$$

The solution to the differential equation (29) assuming the control law given in (30) is

$$h(t) = (h(0) - A)\, e^{\frac{-t}{\tau_T}} + A\, e^{\frac{-t}{\tau_C}} \tag{31}$$

where A is a constant given by

$$A = \frac{\dot{h}(0)\, \tau_T + h(0)}{1 - \frac{\tau_T}{\tau_C}} \tag{32}$$

and $t = 0$ is defined as the time at which the flare or landing phase is initiated. The altitude solution in (31) can be viewed such that $h(0)\, \exp(-t/\tau_T)$ is the desired descent trajectory with a time constant τ_T on the order of the desired time to impact. Furthermore, A is a measure of the difference between the actual descent rate at $t = 0$ and the descent rate required to follow the desired exponential trajectory exactly, which is given by $\dot{h}_{\text{des}} = -h(0)/\tau_T$. Thus, if $\tau_C \ll \tau_T$, the second term of the trajectory solution (31) will decay quickly and may be viewed as a transient correction term for the descent rate. As long as $A < h(0)$, $h(t)$ will always be positive and will approach $h = 0$ exponentially with a time constant of τ_T after the transient term becomes small. This condition on A is guaranteed as long as

$$\dot{h}(0) > \frac{-h(0)}{\tau_C} \tag{33}$$

Thus smaller values of τ_C will result in more robustness to vertical velocity errors at the initiation of flare and landing.

In actual implementation of the acceleration-free control law, the appropriate desired time to impact may be substituted for τ_T based on

Table 2. Autorotation controller parameters

Parameter	Value for AH-1G	Value for TREX 600	Definition
RPM_AUTO	34 rad/s	160 rad/s	Desired main rotor rotation rate for the steady state descent phase
K_D_SS	0.03 s^{-1}	0.003 s^{-1}	Gain on rotor speed time derivative for collective control during steady-state descent
K_P_SS	0.01 (unitless)	0.001 (unitless)	Gain on rotor speed for collective control during steady-state descent
TTI_L	2.0 s	1.0 s	Desired time to impact during the landing phase
TTI_F_MAX	6 s	5 s	Maximum cap on the desired time to impact during the flare phase
K_COL	6.66 $\times 10^{-4}$ rad·s^2/ft	3.1 $\times 10^{-4}$ rad·s^2/ft	Rotor collective gain for flare and landing phases
TAU	0.05 s	0.05 s	Rotor collective adjustment time constant tuning parameter for flare and landing phases
FAST_COL_INCREASE	20 °/s	10 °/s	Collective adjustment rate for rapid adjustments during the flare and landing phases

Table 3. Autorotation controller speed and angle limit parameters

Parameter	Value for AH-1G	Value for TREX 600	Definition
U_TOUCHDOWN	10 ft/s	1 ft/s	Desired forward velocity at touchdown
U_AUTO	100 ft/s	10 ft/s	Desired forward speed for the steady state descent phase
LANDING_MAX_ANGLE	8°	10°	Maximum cap on roll and pitch angles during the landing phase
TOUCHDOWN_MAX_ANGLE	1°	3°	Maximum cap on roll and pitch angles during the touchdown phase
TOUCHDOWN_COL_DECREASE	−1 °/s	−1 °/s	Constant collective pitch rate during touchdown phase

the controller phase, and several parameters (denoted by fixed width font) must be estimated or tuned. The acceleration-free collective control law is given by Eqs. (34) and (35) for the flare and landing phases, respectively (based on Eq. (30)). Note that the gain K_COL is scaled inversely with the square of the rotor rotation speed to correct for the thrust dependency on Ω^2.

Flare:

$$\theta_0 = \mathrm{K\_COL}\frac{\mathrm{NOMINAL\_RPM}^2}{\Omega^2} \times \left(\frac{1}{\mathrm{TAU\_CLIMB}}\left(-\frac{h}{TTI_F} - \dot{h}\right) - \frac{\dot{h}}{TTI_F} + \mathrm{GRAV}\right) \quad (34)$$

Landing:

$$\theta_0 = \mathrm{K\_COL}\frac{\mathrm{NOMINAL\_RPM}^2}{\Omega^2} \times \left(\frac{1}{\mathrm{TAU\_CLIMB}}\left(-\frac{h}{\mathrm{TTI\_L}} - \dot{h}\right) - \frac{\dot{h}}{\mathrm{TTI\_L}} + \mathrm{GRAV}\right) \quad (35)$$

This control law has several drawbacks compared with the version described earlier. First, if the condition in (33) is violated, A will be too large and the velocity correction terms will dominate the response. This is unlikely to lead to a successful vertical trajectory profile. Second, the alternate law relies on the approximate vertical dynamics given in Eq. (29), which may suffer from significant error in some flight conditions (especially in ground effect or highly dynamic inflow conditions). The original control law described earlier only relies on this approximation to determine how fast to adjust θ_0, but seeks the desired acceleration based on feedback measurements, making it significantly more robust. For this reason, if suitable acceleration feedback is available, the original control law is preferred to this alternative.

Velocity tracking controller example implementation

An example velocity-tracking controller implementation is required to evaluate performance of the autorotation controller in both simulation and experiment. The tracking control used here consists of a standard inner-outer loop PD architecture similar to that used in many production helicopter autopilot systems. A detailed block diagram of this controller is omitted here for brevity but may be found in Ref. 18. The outer loop of the velocity-tracking controller generates desired orientation commands ($[\phi_{\mathrm{cmd}}, \theta_{\mathrm{cmd}}, \psi_{\mathrm{cmd}}]^T$) based on u_{des} and the current helicopter velocity. For all the preliminary studies performed here, sideslip angles are regulated to zero and thus $v_{\mathrm{des}} = 0$. The inner loop attempts to track this orientation using the cyclic and tail rotor controls ($[\theta_{1s}, \theta_{1c}, \theta_{\mathrm{tr}}]^T$). Simple modifications may be made to this example controller to include wind corrections from a waypoint generation algorithm if one is available.

Simulation Model

A helicopter simulation model is used to validate the proposed control law based on the ARMCOP model developed by Talbot and Chen (Refs. 19–21). The main rotor model provides increased fidelity over the standard ARMCOP model by incorporating effects from dynamic inflow, ground effect, and blade stall. Detailed descriptions of each model component are omitted for brevity but can be found in the cited references.

Main rotor forces and moments

Forces and moments generated by the main rotor are calculated using a numerical blade element approach in which the main rotor blade is divided into 15 elements and two-dimensional aerodynamic analysis is performed for each. The calculation is repeated at 30 azimuthal stations evenly distributed over a complete revolution and then appropriately averaged and normalized. Main rotor torque is determined by these calculations and used to compute the rotor rotation rate derivative, $\dot{\Omega}$, when the engine is not powering the vehicle. Static stall of the rotor blades is implicitly included in the model through use of a complete aerodynamic lookup table for each blade section (Ref. 22). Dynamic stall and compressibility effects are neglected. Furthermore, first harmonic flapping is assumed and higher harmonic flapping dynamics are neglected for these control law studies. Main rotor flapping states β_0, β_{1s}, and β_{1c} are

included in the vehicle state and propagated using a second-order blade flapping dynamic equation. Further details of the main rotor model are omitted here but are provided in detail in Ref. 18.

Dynamic inflow

A dynamic inflow model is included to increase simulation fidelity in rapidly changing inflow conditions during autorotation. Various dynamic inflow simulation techniques have been developed since the 1980s including linear models (Ref. 23), free-vortex wake models (Ref. 24), and state-space wake models derived from indicial theory (Ref. 25). These models range in complexity, but the relatively simple linear model structure developed by Peters et al. (Ref. 23) is used most often in flight dynamic studies. However, free-vortex wake models likely provide higher accuracy, especially in turbulent wake conditions such as those experienced during autorotation, at the expense of significant computational burden. Owing to the requirement for extensive Monte Carlo simulation in this study, the Pitt and Peters dynamic inflow model described in Refs. 26 and 27 was selected for use here as a reasonable trade-off between accuracy and computational complexity. The model has three states, λ_0, λ_s, and λ_c, which describe the induced inflow ratio distribution over the rotor disk according to the equation

$$\lambda_i(r, \psi_{\text{MR}}) = \lambda_0 + \lambda_s \frac{r}{R} \sin\psi_{\text{MR}} + \lambda_c \frac{r}{R} \cos\psi_{\text{MR}} \tag{36}$$

These states evolve according to the dynamic equation

$$[M] \begin{bmatrix} \dot{\lambda}_0 \\ \dot{\lambda}_s \\ \dot{\lambda}_c \end{bmatrix} + [\hat{L}]^{-1} \begin{bmatrix} \lambda_0 \\ \lambda_s \\ \lambda_c \end{bmatrix} = \mathbf{C} \tag{37}$$

where $\mathbf{C}$ is the vector of body frame force and moment coefficients calculated using the blade element approach described above, $[\hat{L}]$ is a matrix dependent on the sideslip angle and wake angle, and $[M]$ is a mass term based on the mass of air near the rotor. Additional details regarding this model can be found in Ref. 27.

Ground effect

A simple ground effect correction is applied to the dynamic inflow model when the vehicle is in close proximity to the ground. Equation (37) shows that when the inflow has reached steady state (i.e., $\dot{\lambda} = \mathbf{0}$),

$$\mathbf{C} = [\hat{L}]^{-1} \lambda_{\mathbf{ss}} \tag{38}$$

where $\lambda_{\mathbf{ss}}$ is the vector of the inflow states at steady state. It is assumed that in ground effect the steady-state inflow can be modeled by

$$\lambda_{\mathbf{ssIGE}} = \left(1 - 0.8 \frac{\Delta w}{w_0}\right) \lambda_{\mathbf{ss}} \tag{39}$$

where $\Delta w/w_0$ is a correction term for ground effect in forward flight described by Heyson (Ref. 28). The correction terms calculated in Ref. 28 are only valid at the center of the rotor and decrease spanwise along the blade (Ref. 29). Therefore, an average value of 80% of the $\Delta w/w_0$ value reported in Ref. 28) is used over the entire rotor. This correction term is applied in the dynamic inflow model by adjusting $\mathbf{C}$ so that λ tends toward $\lambda_{\mathbf{ssIGE}}$. At steady state,

$$\mathbf{C_{IGE}} = [\hat{L}]^{-1} \lambda_{\mathbf{ssIGE}} \tag{40}$$

$$= [\hat{L}]^{-1} \left(1 - 0.8 \frac{\Delta w}{w_0}\right) \lambda_{\mathbf{ss}} \tag{41}$$

$$= [\hat{L}]^{-1} [\hat{L}] \left(1 - 0.8 \frac{\Delta w}{w_0}\right) \mathbf{C} \tag{42}$$

$$\mathbf{C_{IGE}} = \left(1 - 0.8 \frac{\Delta w}{w_0}\right) \mathbf{C} \tag{43}$$

In the dynamic inflow equation (37), $\mathbf{C}$ is adjusted using Eq. (43) when the main rotor is within two rotor diameters of the ground:

$$[M] \begin{bmatrix} \dot{\lambda}_0 \\ \dot{\lambda}_s \\ \dot{\lambda}_c \end{bmatrix} + [\hat{L}]^{-1} \begin{bmatrix} \lambda_0 \\ \lambda_s \\ \lambda_c \end{bmatrix} = \left(1 - 0.8 \frac{\Delta w}{w_0}\right) \mathbf{C} \tag{44}$$

The values for $\Delta w/w_0$ are taken from a lookup table based on Ref. 28, and data are indexed based on the height above ground and the wake angle determined from the inflow state and velocity of the helicopter.

Simulation overview

The fuselage, horizontal and vertical stabilizer, and tail rotor components of the helicopter model provide additional aerodynamic forces. The tail rotor uses Newton–Raphson iteration to calculate uniform tail rotor inflow, and blade flapping is assumed to be quasi-steady. The tail rotor and main rotor rotation rates are coupled through use of a scale factor. Fuselage and stabilizer components use linear aerodynamic models, and downwash components are included through a simplified fuselage drag model. Details regarding these contributions to the total helicopter forces and moments may be found in Ref. 19. Furthermore, actuator rate limits are imposed in the simulation as well as maximum and minimum stops. Actuator rate limits are set to 40 deg/s and are imposed on θ_0, θ_{1s}, θ_{1c}, and θ_{tr} (note this limit applies to the actuator response and not the controller demand).

The net force on the helicopter (F_x, F_y, and F_z) and the net moment about the mass center (M_x, M_y, and M_z) are composed of contributions from the main rotor, tail rotor, fuselage and empennage aerodynamics, and weight. Net force and moment components are expressed in the helicopter body frame and drive the six degree-of-freedom rigid body equations that govern helicopter motion. These equations of motion are integrated forward in time using a fourth-order Runge–Kutta algorithm with a timestep of 0.001 s. Note that the entire vehicle state vector is composed of the 12 rigid body vehicle states, main rotor rotation rate, three dynamic inflow states, three flapping angles, and three flapping angle rates.

Simulation Results

Example and Monte Carlo simulations are performed to characterize control law performance under different flight conditions. Similar simulation experiments are conducted for both the AH-1G Cobra helicopter and for the R/C-sized Align TREX 600 model helicopter.

Bell AH-1G Cobra simulations

Model parameters used for the AH-1G simulations are obtained from Ref. 19. Table 4 lists some of the important model parameters. All feedback states are perturbed with Gaussian white noise to simulate measurement error, and Table 4 provides measurement error standard deviations. Tables 2, 3, and 5 list the controller parameters used for these tests.

Table 4. Select model parameters for the Bell AH-1G simulation

Parameter	Symbol	Value
Helicopter gross weight	W	8300 lb
Number of main rotor blades	N_b	2 (teetering)
Main rotor blade chord	c	2.25 ft
Main rotor radius	R	22 ft
Main rotor blade moment of inertia	I_B	2770 slug ft^2
Main rotor height above ground (water line)	WL_MR	12.73 ft
Main rotor normal operating speed	Ω_{normal}	32.88 rad/s
Main rotor blade airfoil used for simulation		NACA 0012
Actuator max rate	$\dot{\delta}_{\max}$	40 deg/s
Controller update rate		100 Hz
Velocity sensor noise standard deviation	σ_{vel}	1.0 ft/s
Acceleration sensor noise standard deviation	σ_{accel}	3.0 ft/ s^2
Attitude sensor noise standard deviation	σ_{attitude}	1.5 deg
Attitude rate sensor noise standard deviation	σ_{rate}	3.0 $^\circ$/s
Altitude sensor noise standard deviation	σ_h	1.0 ft
Climb rate sensor noise standard deviation	$\sigma_{\dot{h}}$	1.0 ft/s

Table 5. Flight phase fuzzy transitions for the AH-1G Cobra helicopter

Transition	Altitude Range (ft)	Time-to-Impact Range (s)
Steady state descent to preflare	200–250	5–7
preflare to flare	30–70	3–3.5
Flare to landing	5–15	0.5–1.2
Landing to touchdown	0–2	0–0.1

Since trapezoidal membership functions are used, transitions are linear.

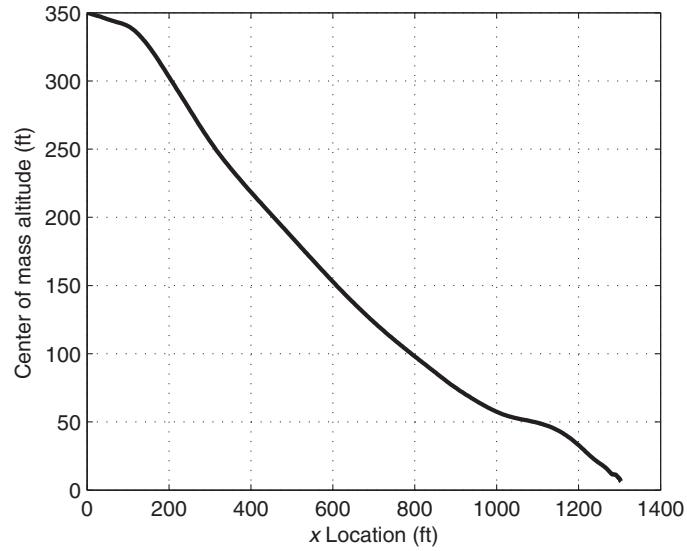

Fig. 3. Example AH-1 distance versus altitude flight profile.

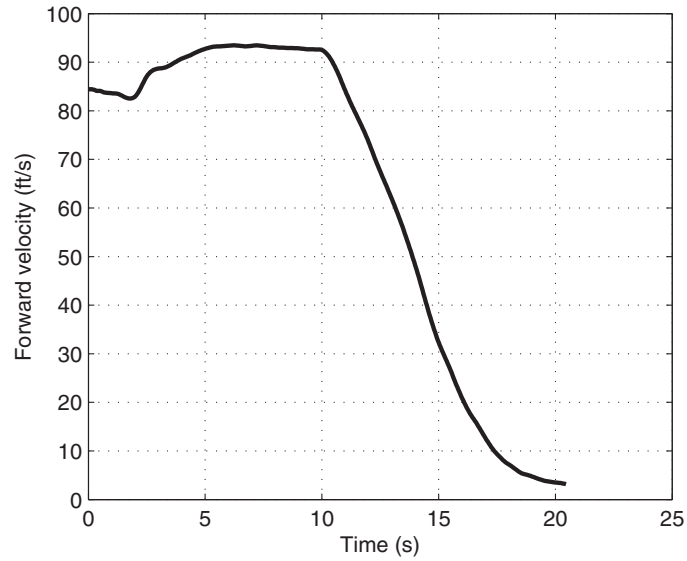

Fig. 4. Example AH-1 body frame velocity history.

An example simulation is performed in which autorotation is initiated from a trimmed flight condition at an altitude of 350 ft, forward speed of 50 kt, and gross weight of 8300 lb. A 1-s delay between engine shutoff and the point at which the autorotation controller takes over from the normal flight controller is simulated, representing the actual time it would potentially take to confirm power loss and initiate the autorotation controller. Figure 3 shows a distance versus altitude flight profile, and Figure 4 shows a time history of body frame velocity u. Note that although the initial state is near the edge of the avoid region of the AH-1G's H–V diagram, the controller handles the maneuver well and brings the vehicle to a safe landing. The vehicle achieves the desired forward speed for the minimum descent rate of approximately 90 ft/s. A time history of the vehicle pitch angle, not included here, shows that initially the controller commands a pitch forward maneuver to increase forward speed, followed by a 20–25 deg pitch-up maneuver during flare. The vehicle pitches down to an approximately level attitude just after 20 s. Figure 5 provides a time history of the rotor rotation rate, showing an immediate drop in the rotor rotation rate before the autorotation controller takes effect followed by the return of Ω to a value slightly higher than the normal operating value during steady-state descent. A time history of the main rotor collective is also shown in Fig. 5. Finally, Figs. 6 and 7 show time histories of the phase control authority and time-to-impact internal variables. Note that for clarity in presentation, the constant velocity time-to-impact shown in this figure is calculated without sensor noise although the controller actually uses the noise-perturbed value. Also note that *TTLE* can be derived from the plotted results in Fig. 7 as the difference between TTI_F and `TTI_L`. For the example case considered here, total horizontal velocity and vertical velocity at touchdown are 3.7 and 3.9 ft/s, respectively, whereas pitch and roll angles at touchdown are nearly level at -1.5° and -0.7° respectively.

Monte Carlo simulations are also conducted using initial conditions in and around the "avoid" region of the H–V diagram to demonstrate that the controller is able to recover from difficult (low-energy) initial conditions. To capture the effects of controller handoff delays on controller performance, Monte Carlo simulations are performed using various delay values between the failure event (engine failure, tail rotor failure, etc) and initiation of the autorotation controller. Typical handoff delays for certification purposes are 1–2 s depending on pilot workload (Ref. 1). In each Monte Carlo simulation, performance is evaluated based on the state of the helicopter upon impact with the ground. Conditions for "successful," "marginal," and "crash" landings are specified in Table 6. "Successful" landing conditions are designed to represent a landing which would likely cause no damage to the aircraft, whereas "marginal" landing conditions would likely result in damage to the aircraft but be survivable to passengers and equipment. Note that potential tail strikes are also recorded

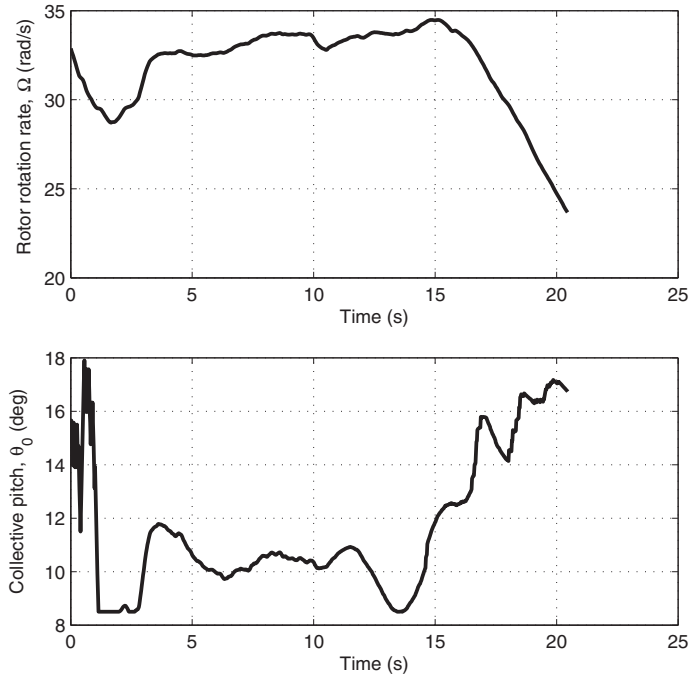

Fig. 5. Example AH-1 rotor rotation rate and collective pitch histories.

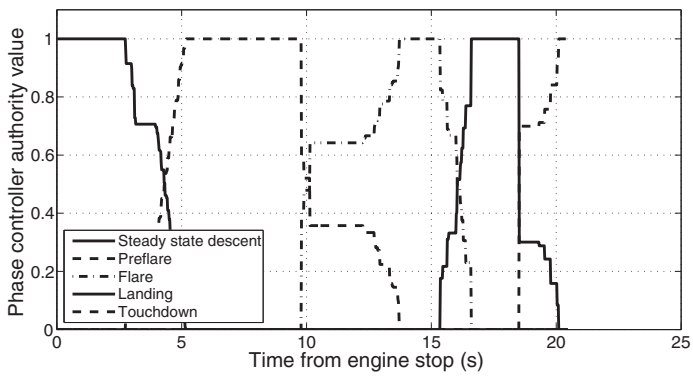

Fig. 6. Example AH-1 phase control authority history.

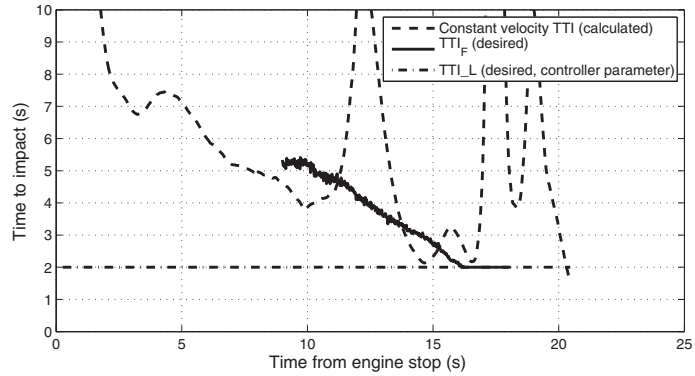

Fig. 7. Example AH-1 time-to-impact parameters history.

Table 6. Conditions for successful and marginal landings for the AH-1G

Parameter	Condition for Successful Landing	Condition for Marginal Landing
Roll angle, ϕ	$<5^\circ$	$<10^\circ$
Pitch angle, θ	$-5^\circ < \theta < 10^\circ$	$-5^\circ < \theta < 15^\circ$
Forward speed, $\dot{x}$	<20 kt	<40 kt
Lateral speed, $\dot{y}$	<3 ft/s	<6 ft/s
Vertical speed, $\dot{z}$	<8 ft/s	<15 ft/s
Roll rate, p	$<8\ ^\circ$/s	$<15\ ^\circ$/s
Pitch rate, q	$<10\ ^\circ$/s	$<20\ ^\circ$/s
Yaw rate, r	$<8\ ^\circ$/s	$<15\ ^\circ$/s

Simulations that do not meet these criteria are considered crashes (conditions applied to absolute value of parameter unless otherwise noted).

and incorporated into the Monte Carlo analysis, where tail strikes during landing are computed based on the orientation of the aircraft and tail boom length. If a tail strike is detected in a landing otherwise categorized as "successful," the category is changed to "marginal."

Figure 8 shows the results of 1000 simulated autorotation landings with an immediate handoff, and Figure 9 shows results using a handoff delay of 2 s. Each solid dot represents a successful landing from the indicated position, and a diamond indicates a marginal category landing. A $\times$ symbol indicates a crash. The low-speed "avoid" region of the H–V diagram for the AH-1G Cobra is also marked for reference (Ref. 30), although it is important to note that this avoid region captures pilot comfort level and thus is expected to be more conservative than the region in which the controller can successfully land the helicopter. Note that the controller is able to perform a safe autorotation in the vast majority of cases except in helicopter states where the total vehicle energy (sum of kinetic and potential energies) at autorotation initiation is low. The majority of marginal or crash landings in the avoid region occur due to violation of the vertical velocity criteria. Also note that, in general, performance suffers as the handoff delay grows which is expected. At low initial energies, the controller does not have time to build up main rotor rpm and instead must initiate the flare maneuver immediately with less available thrust, leading to higher ground impact speeds. Other Monte Carlo cases, not shown here, demonstrate that controller performance in overweight scenarios (gross weight of 9000 lb) with a 1-s delay largely mirrors performance at a gross weight value of 8300 lb with a 2-s delay. Thus, as expected, higher disk loading reduces the controller's margin for error but performance is still generally satisfactory. The few marginal landing outlier cases outside the avoid region in Figs. 8 and 9 showed impact conditions that exceeded the successful criteria by only a very small amount. Also note that the majority of cases in Figs. 8 and 9 yielded pitch angles at impact between -1 and 1 deg. It is possible that by adding an additional constraint prohibiting negative pitch angles in the landing and touchdown phases, the controller would be biased toward positive pitch angles and negative values may be avoided entirely, although such additions are not explored here.

In all tests, the controller generally has difficulty at high forward flight speeds and low altitude (below 40 ft). This is typically a dangerous region of the height–velocity envelope since there is usually insufficient time to slow the helicopter to a safe speed before ground impact and insufficient altitude to establish a steady-state descent. Suitable performance in such scenarios would likely require an immediate open-loop climb command to gain altitude, followed by initiation of the standard autorotation descent beginning with the steady-state descent phase. This mimics typical high-speed low-altitude autorotation maneuvers carried out by human pilots

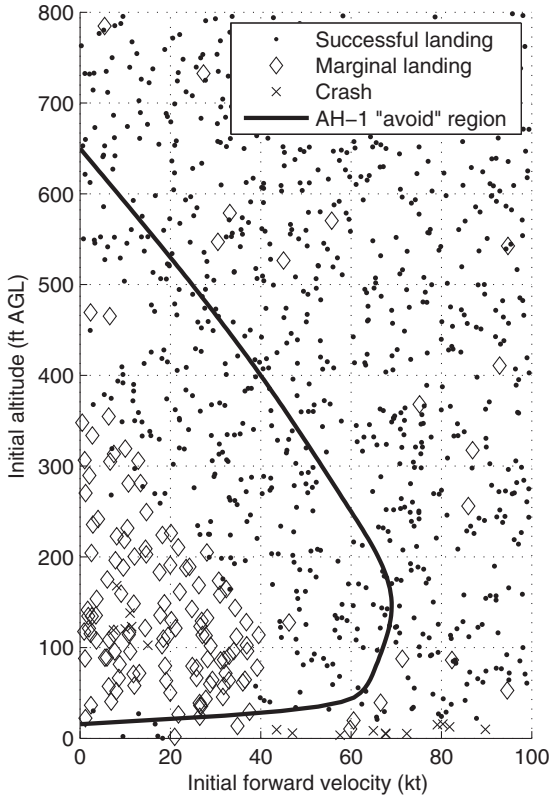

Fig. 8. AH-1 Monte Carlo test results (immediate handoff).

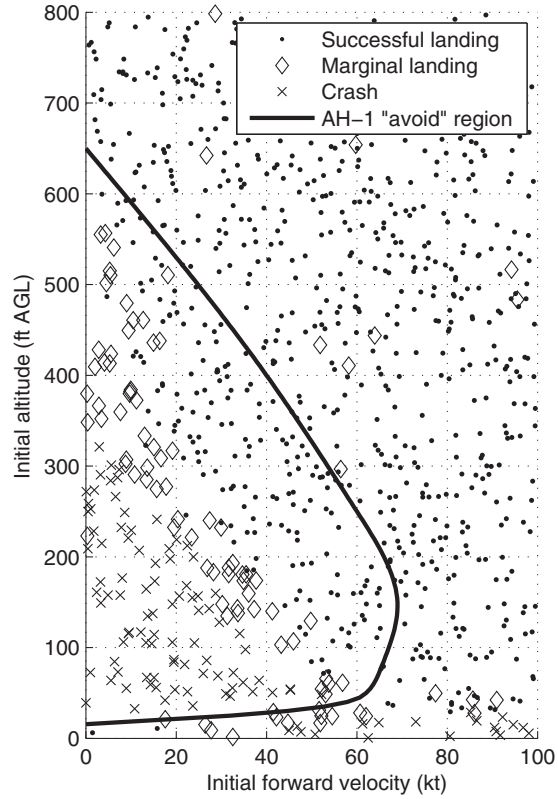

Fig. 9. AH-1 Monte Carlo test results (2-s handoff delay).

(Ref. 1). Such additions to the autorotation control framework are not explored here but may improve performance in this specific flight regime. These modifications, potentially involving backward progression through the control phases, are left to future work.

Align TREX 600 simulations

Simulations are also performed using a model of the Align TREX 600 hobby-class helicopter to demonstrate controller portability. The simulation has a similar structure to the AH-1G model, with simulation parameters listed in Table 7. The Align TREX uses a semirigid rotor hub in which blades do not have a flapping degree of freedom. Thus the model is modified to incorporate an equivalent hinge offset and hub spring (Ref. 1).

An example simulation is shown in which autorotation is initiated from an altitude of 100 ft and forward speed of 10 ft/s. As before, a 1-s delay between engine shutoff and the point at which the autorotation controller takes over from the normal flight controller is used. Figure 10 shows a distance versus altitude flight profile, and Fig. 11 shows a time history of body frame velocity u. Note that the autorotation is completed in approximately 7 s, and touchdown occurs with nearly zero forward speed and vertical speed of less than 5 ft/s. As in the Cobra simulations, a time history of vehicle pitch angle is not shown but generally indicates a similar trend of a pitch forward maneuver followed by a pitch back maneuver during flare. Touchdown is initiated at a pitch angle of less than 1 deg and a roll angle of less than 5 deg. Figure 12 shows a time history of Ω as well as main rotor collective, where the 1-s handoff delay is clearly present. Note that minimum collective (negative for the aerobatic model helicopter) is commanded immediately during the steady-state descent phase and maximum collective is commanded near touchdown to slow the descent. Finally, Fig. 13 shows time-to-impact internal variables, indicating similar trends as in the AH-1G example case. Performance demonstrated in this example case would certainly be survivable for this model aircraft.

Table 7. Align TREX 600 model parameters pertaining to autorotation

Parameter	Symbol	Value
Helicopter gross weight	W	8.15 lb
Number of main rotor blades	N_b	2 (semirigid hub)
Main rotor blade chord	c	0.1771 ft
Main rotor radius	R	2.208 ft
Main rotor blade moment of inertia	I_B	0.01357 slug ft^2
Main rotor height above ground (water line)	WL_MR	1.5 ft
Main rotor normal operating speed	Ω_normal	162 rad/s
Main rotor blade airfoil used for simulation		NACA 0012
Actuator max rate	$\dot{\delta}_{max}$	100 deg/s
Controller update rate		100 Hz
Velocity sensor noise standard deviation	σ_vel	1.0 ft/s
Acceleration sensor noise standard deviation	σ_accel	3.0 ft/ s^2
Attitude sensor noise standard deviation	$\sigma_{attitude}$	1.5 deg
Attitude rate sensor noise standard deviation	σ_{rate}	3.0 °/s
Altitude sensor noise standard deviation	σ_h	0.2 ft
Climb rate sensor noise standard deviation	$\sigma_{\dot{h}}$	0.5 ft/s

Monte Carlo simulations are performed using the TREX 600 model to demonstrate the controller's effectiveness in a wide variety of initial flight conditions. Landings are classified according to the criteria listed in Table 8. Figures 14 and 15 show landing performance with an immediate handoff and a 3-s handoff delay, respectively. When the handoff delay is

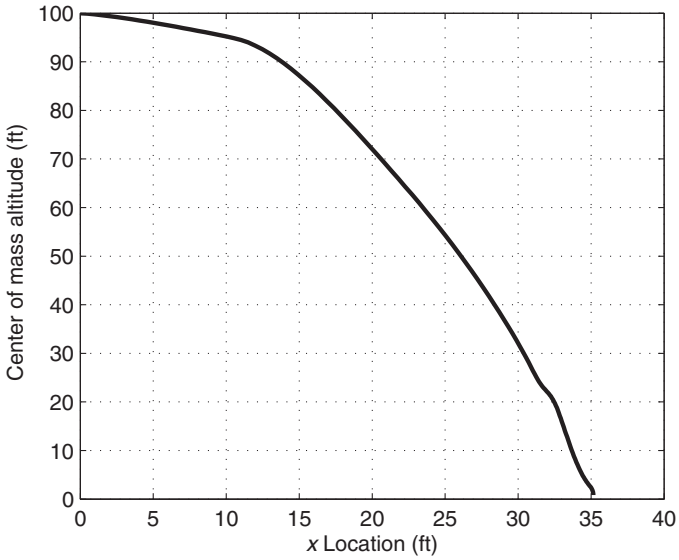

Fig. 10. Example TREX 600 distance versus altitude flight profile.

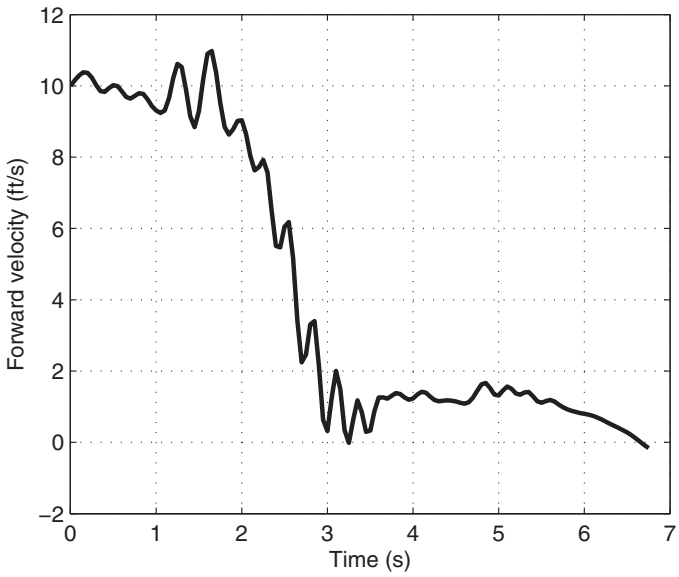

Fig. 11. Example TREX 600 body frame velocity history.

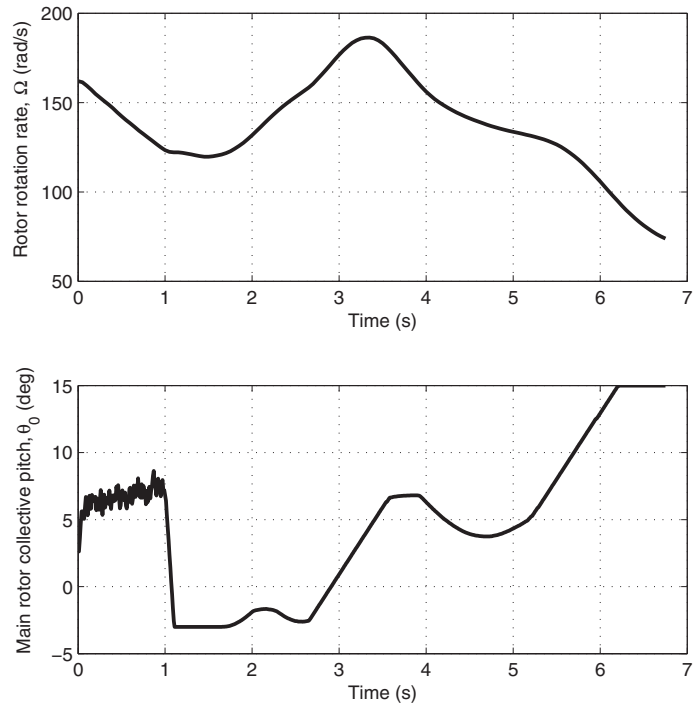

Fig. 12. Example TREX 600 rotor rotation rate and collective pitch histories.

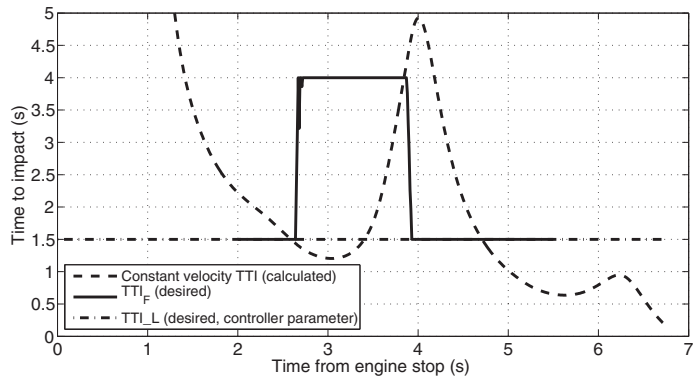

Fig. 13. Example TREX 600 time to impact parameter history.

small, the controller is able to handle a wide variety of initial conditions. As the handoff delay is increased, performance becomes progressively worse due to the decrease in rotor rpm caused by the controller attempting to maintain altitude before the handoff. Additional Monte Carlo results were generated with a 50% increase in vehicle gross weight (not shown here). Performance in this increased-weight case was similar to controller performance with the nominal gross weight using a 1-s handoff delay. Overall, when combined with the AH-1G results, Figures 10–15 demonstrate reasonable performance of the autorotation controller when applied to vehicles of various scales.

Flight Test

A limited set of flight experiments was conducted to demonstrate controller performance given realistic measurement feedback and disturbances. A small R/C helicopter, the Align TREX 600e, was used for these flight tests. For these preliminary flight experiments, trajectories were limited to vertical autorotation only and thus validation of the forward flight component of the autorotation controller is left to future experiments. Furthermore, limitations in the quality of accelerometer feedback led to use of the acceleration-free version of the flare and landing control laws discussed in the Controller Design section.

Flight test setup and methodology

The controller parameter values used in the flight experiments were similar to those shown in Table 2. The additional acceleration-free controller parameters used in the flight tests are given by $\texttt{K\_COL} = 1524$ rad s^2/ ft, $\texttt{TAU\_CLIMB} = 0.25$ s, and $\texttt{GRAV} = 65.6$ ft/s^2. The autopilot used for the flight experiments was an ArduPilot model 2.5.2, which consists of an ATmega2560 8-bit microprocessor running at 16 MHz coupled with a sensor package. These sensors include a three-axis magnetometer, barometric altimeter, GPS, three-axis accelerometer,

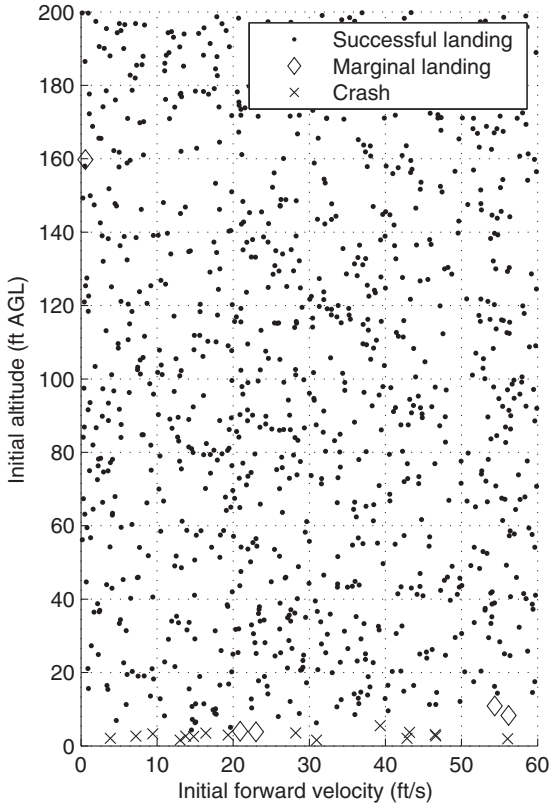

Fig. 14. TREX 600 Monte Carlo Test results (immediate handoff).

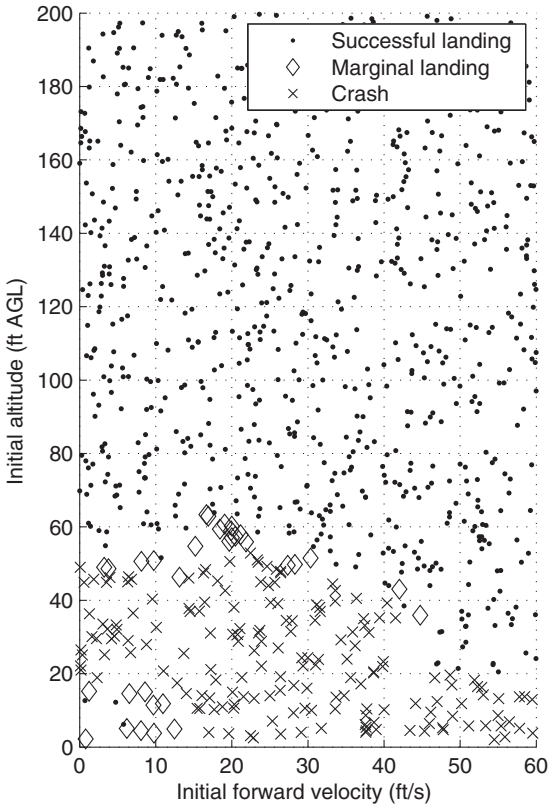

Fig. 15. TREX 600 Monte Carlo test results (3-s handoff delay).

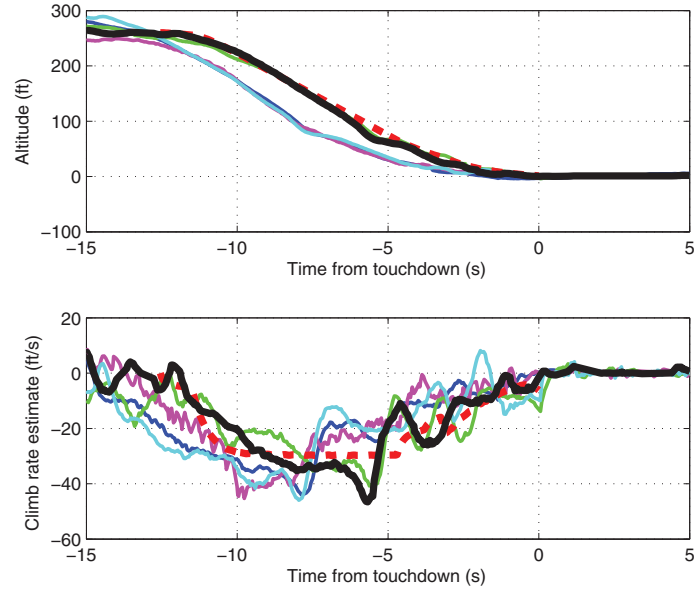

Fig. 16. Altitude versus time and vertical speed versus time. Solid lines are experimental data, a dark solid line is the experimental case highlighted in the Discussion, and a dashed line is the simulated one.

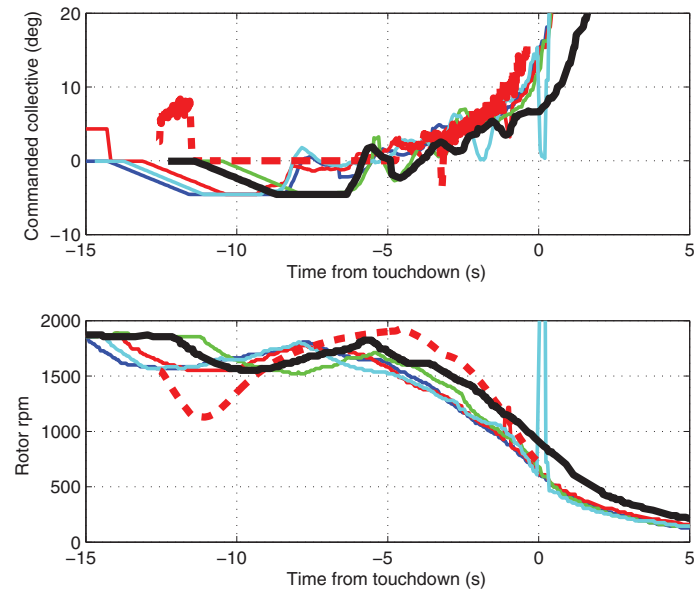

Fig. 17. Collective pitch versus time and rotor rotation rate versus time. Solid lines are experimental data, a dark solid line is the experimental case highlighted in the Discussion, and the dashed line is simulated.

and three-axis gyroscope. In addition, the aircraft was outfitted with a custom rotor rpm sensor and a downward-facing ultrasonic sensor for measuring precise ground proximity. A Kalman filter with outlier rejection was implemented to combine altimeter and ultrasonic sensor measurements.

The velocity-tracking controller used in the flight experiments has structure similar to that described earlier except that a waypoint-tracking loop was included to generate commands for u_{des} and v_{des}. This allows wind corrections to be included in the feedback control structure but has negligible effect on autorotation controller performance. During

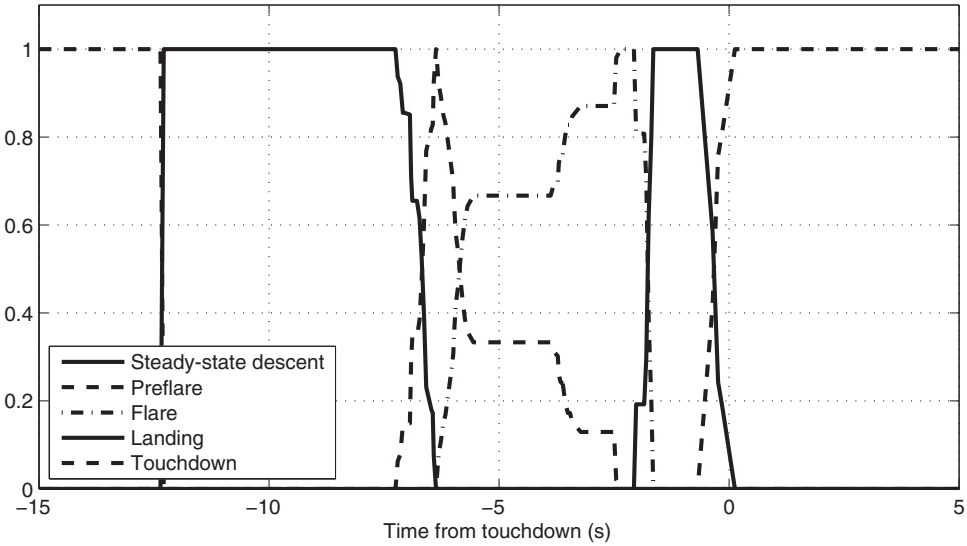

Fig. 18. Phase progression for selected autorotation flight test.

Table 8. Conditions for successful and marginal landings for the TREX 600

Parameter	Condition for Successful Landing	Condition for Marginal Landing
Roll angle, ϕ	$<5^\circ$	$<10^\circ$
Pitch angle, θ	$-5^\circ < \theta < 10^\circ$	$-5^\circ < \theta < 15^\circ$
Forward speed, $\dot{x}$	<6 ft/s	<12 ft/s
Lateral speed, $\dot{y}$	<5 ft/s	<6 ft/s
Vertical speed, $\dot{z}$	<7 ft/s	<12 ft/s
Roll rate, p	<10 °/s	<15 °/s
Pitch rate, q	<10 °/s	<20 °/s
Yaw rate, r	<8 °/s	<15 °/s

Simulations that do not meet these criteria are considered crashes (conditions applied to absolute value of parameter unless noted).

autorotation tests, a single waypoint is set at the horizontal location of autorotation entry so that the vehicle will follow a vertical path to the ground. The velocity-tracking controller is tuned for waypoint following in powered flight, and thus the success of these flight experiments demonstrates how the autorotation controller is highly compatible with existing autopilot control laws.

Flight-test results

Several flight experiments were performed from an initial altitude of 250 ft above ground level. Starting from a trimmed flight condition, the helicopter's motor was powered off and the vehicle landed completely autonomously. Numerous trials were conducted, which were largely successful. Figure 16 shows a time history of altitude and vertical speed for five selected trials. Both of these data sets are derived from the Kalman filter estimates and thus do not represent truth measurements. Throughout all figures, an example time history is highlighted using a thicker black line for discussion purposes. A simulation time history is also shown with a dashed line. This simulation was run from approximately the same initial conditions as the flight tests and used the acceleration-free version of the control law. Figure 17 shows time histories of collective inputs and main rotor rpm, and Fig. 18 shows a controller phase time history for the example trajectory highlighted in black.

Several features are noteworthy in these results and were evident in further trials not shown here. First, the controller is able to successfully land the helicopter in engine-out scenarios, demonstrating vertical velocities at touchdown of under 3 ft/s in most cases, which is well below the damage threshold for the helicopter. Second, note that shortly after engine cutoff collective is commanded full negative, which yields an rpm increase nearly back to the nominal value for power-on flight. As the aircraft nears the ground collective is gradually increased causing a reduction in rotor rpm as expected. The helicopter consistently impacts the ground with a rotor rotation rate of 30–50% of the nominal value. Note that, for this small helicopter, this rotor rotation rate is still enough for minor cyclic adjustments and reasonable margin of error (for full-sized helicopters with larger rotor inertia, the decay as a percentage of the nominal rate would be less as shown in Fig. 5). Third, note that the simulated trajectory and experimental data show reasonable correlation, lending credibility to the simulation results provided above. Finally, it was observed that there was significant interaction between transient inflow dynamics and altitude measurements from the barometer (which was necessarily placed under the rotor as there was no suitable alternative location). Thus, as shown in the example case around 6 s from impact, sudden increases in collective pitch generated momentary high pressure at the barometric sensor due to increased induced velocity. This type of spurious measurement caused occasional spikes in vertical velocity feedback, which were mitigated to some extent using shielding around the autopilot sensor package (although this effect was never fully eliminated). Overall, upward of 10 successful vertical autorotations were performed in wind conditions exceeding 10 kt, validating the overall control system design in a realistic environment.

Concluding Remarks

A novel expert system control law for autonomous autorotation has been proposed and validated through simulation and limited experimental tests. The multiphase control structure incorporates estimates of the time-to-ground impact using a simple kinematic model, enabling suitable flare trajectories to be calculated quickly in a feedback manner. Through calculation of a desired time to impact, flare trajectories are furthermore conditioned based on the total kinetic energy available for

maneuver. The controller is designed for straightforward integration with existing autopilots, landing site selection algorithms, and pilot guidance. Simulations and limited experimental data validate the control algorithm and show suitable performance in realistic environments. Overall, results demonstrate the portability of the proposed controller as well as its potential use as an automated autorotation landing system for single engine rotorcraft.

Acknowledgments

The authors thank Bradley Taylor for helping to develop the simulation software used in this research, Lee Fowler for piloting the flight-test helicopter, and Robert Long for creating flight-test electronics. This material is based on work supported by the National Science Foundation, Grant No. 1252521.

References

[1]Leishman, J. G., *Principles of Helicopter Aerodynamics*, Cambridge University Press, New York, 2006.

[2]Johnson, W., "Helicopter Optimal Descent and Landing after Power Loss," TM-73244, NASA, 1977.

[3]Lee, A. Y., Bryson, A. E., and Hindson, W. S., "Optimal Landing of a Helicopter in Autorotation," *Journal of Guidance, Control, and Dynamics*, Vol. 11, (1), 1988, pp. 7–12.

[4]Hazawa, K., Shin, J., Fujiwara, D., Igarashi, K. Fernando, D., and Nonami, K., "Autonomous Autorotation Landing of Small Unmanned Helicopter," *Transactions of the Japan Society of Mechanical Engineers*, Vol. 70, (698), 2004, pp. 2862–2869.

[5]Abbeel, P., Coates, A., Hunter, T., and Ng, A. Y., "Autonomous Autorotation of an RC helicopter," *Experimental Robotics*, Vol. 54, 2009, pp. 385–394.

[6]Dalamagkidis, K., Valavanis, K. P., and Piegl, L. A., "Autonomous Autorotation of Unmanned Rotorcraft using Nonlinear Model Predictive Control," *Journal of Intelligent and Robotic Systems*, Vol. 57, (1–4), September 2009, pp. 351–369.

[7]Dooley, L. W., and Yeary, R. D., "Flight Test Evaluation of the High Inertia Rotor System," USARTL-TR-79-9, US Army Research and Technology Laboratories, June 1979.

[8]Yomchinda, T., Horn, J. F., and Langelaan, J. W., "Flight Path Planning for Descent-Phase Helicopter Autorotation," AIAA-2011-6601, AIAA Guidance, Navigation, and Control Conference, Portland, OR, August 8–11, 2011, pp. 1–24.

[9]Tierney, S., and Langelaan, J., "Autorotation Path Planning Using Backwards Reachable Set and Optimal Control," AHS International 66th Annual Forum Proceedings, Phoenix, AZ, May 11–13, 2010.

[10]Keller, J. D., McKillip, Jr., R. M., Horn, J. F., and Yomchinda, T., "Active Flight Control and Appliqué Inceptor Concepts for Autorotation Performance Enhancement," AHS International 67th Annual Forum Proceedings, Virginia Beach, VA, May 3–5, 2011.

[11]Bachelder, E. N., Lee, D.-C., and Aponso, B. L., "Autorotation Flight Control System," U.S. Patent 7976310 B2, 2011.

[12]Padfield, G., Lee, D., and Bradley, R., "How Do Helicopter Pilots Know When to Stop, Turn, or Pull Up," *Journal of the American Helicopter Society*, Vol. 48, (2), 2003, pp. 108–109.

[13]Padfield, G., Clark, G., and Taghizad, A., "How Long Do Pilots Look Forward? Prospective Visual Guidance in Terrain-Hugging Flight," *Journal of the American Helicopter Society*, Vol. 52, (2), 2007, pp. 134–145.

[14]Padfield, G. D., Lu, L., and Jump, M., "Tau Guidance in Boundary-Avoidance Tracking: New Perspectives on Pilot-Induced Oscillations," *Journal of Guidance, Control, and Dynamics*, Vol. 35, (1), January 2012, pp. 80–92.

[15]Jump, M., and Padfield, G., "Investigation of the Flare Maneuver Using Optical Tau," *Journal of Guidance, Control, and Dynamics*, Vol. 29, (5), 2006, pp. 1189–1200.

[16]Livchitz, M., Abershitz, A., Soudak, U., and Kandel, A., "Development of an Automated Fuzzy-logic-based Expert System for Unmanned Landing," *Fuzzy Sets and Systems*, Vol. 93, (2), 1998, pp. 145–159.

[17]Yen, J., and Langari, R., *Fuzzy Logic: Intelligence, Control, and Information*, Pearson Education, Zug, Switzerland, 1999.

[18]Sunberg, Z., "A Real Time Expert Control System For Helicopter Autorotation," Master's Thesis, Texas A&M University, College Station, TX, 2013.

[19]Talbot, P. D., Tinling, B. E., Decker, W. A., and Chen, R. T. N., "A Mathematical Model of a Single Main Rotor Helicopter for Piloted Simulation," TM-84281, NASA, 1982.

[20]Chen, R. T. N., "A Simplified Rotor System Mathematical Model for Piloted Flight Dynamics Simulation," TM-78575, NASA, May 1979.

[21]Chen, R. T. N., "Effects of Primary Rotor Parameters on Flapping Dynamics," Technical Paper TP-1431, NASA Ames Research Center, January 1980.

[22]Sheldahl, R. E., and Klimas, P. C., "Aerodynamic Characteristics of Seven Symmetrical Airfoil Sections through 180-degree Angle of Attack for Use in Aerodynamic Analysis of Vertical Axis Wind Turbines," SAND-80-2114, Sandia National Laboratories, Albuquerque, NM, March 1981.

[23]Peters, D., Boyd, D., and He, C., "Finite-State Induced-Flow Model for Rotors in Hover and Forward Flight," *Journal of the American Helicopter Society*, Vol. 34, (4), October 1989, pp. 5–17.

[24]Celi, R., "State-Space Representation of Vortex Wakes Using the Method of Lines," *Journal of the American Helicopter Society*, Vol. 50, (2), April 2005, pp. 195–205.

[25]Johnson, W., "Time-Domain Unsteady Aerodynamics of Rotors with Complex Wake Configurations," *Vertica*, Vol. 12, 1988, pp. 83–100.

[26]Pitt, D. M., and Peters, D. A., "Theoretical Prediction of Dynamic-Inflow Derivatives," *Vertica*, Vol. 6, 1981, pp. 21–34.

[27]Peters, D. A., and HaQuang, N., "Dynamic Inflow for Practical Applications," *Journal of the American Helicopter Society*, Vol. 33, (4), October 1988, pp. 64–68.

[28]Heyson, H. H., "Ground Effect for Lifting Rotors in Forward Flight," Technical Note D-234, NASA, May 1960.

[29]Knight, M., and Hefner, R. A., "Analysis of Ground Effect on the Lifting Airscrew," Technical Note TN-835, NACA, Washington, DC, December 1941.

[30]Free, L. M., and Hepler, L. J., "Height-Velocity Test: AH-1G Helicopter at Heavy Gross Weight," USAASTA Project No. 74-19, U.S. Army Aviation Systems Command, Edwards AFB, CA, June 1974.